Published in final edited form as:
Phys Med Biol. 2011 July 7; 56(13): 4041–4057. doi:10.1088/0031-9155/56/13/019.

Monitoring proton radiation therapy with in-room PET imaging

Xuping Zhu, Ph.D.[1], **Samuel España, Ph.D.**[2,3], **Juliane Daartz, Ph.D.**[2,4], **Norbert Liebsch, M.D., Ph.D.**[2], **Jinsong Ouyang, Ph.D.**[1], **Harald Paganetti, Ph.D.**[2], **Thomas R Bortfeld, Ph.D.**[2], and **Georges El Fakhri, Ph.D.**[1]

[1]Department of Imaging, MGH and Harvard Medical School, Boston, MA 02114, USA.
[2]Department of Radiation Oncology, MGH and Harvard Medical School, Boston, MA 02114, USA.
[3]Now with MEDISIP, Department of Electronics and Information Systems, Ghent University-IBBT-IBiTech, Ghent, Belgium. [4]Now with Paul Scherrer Institute, 5232 Villigen PSI, Switzerland.

Abstract

Purpose—We used a mobile PET scanner positioned within the proton therapy treatment room to study the feasibility of proton range verification with an in-room, stand-alone PET system, and compared with off-line equivalent studies.

Methods and materials—Two subjects with adenoid cystic carcinoma were enrolled into a pilot study in which in-room PET scans were acquired in list-mode after a routine fractionated treatment session. The list-mode PET data were reconstructed with different time schemes to generate in-room short, in-room long and off-line equivalent (by skipping coincidences from the first 15 minutes during the list-mode reconstruction) PET images for comparison in activity distribution patterns. A phantom study was followed to evaluate the accuracy of range verification for different reconstruction time schemes quantitatively.

Results—The in-room PET has a higher sensitivity compared to the off-line modality so that the PET acquisition time can be greatly reduced from 30 min to <5 min. Features in deep-site, soft-tissue regions were better retained with in-room short PET acquisitions because of the collection of ^{15}O component and lower biological washout. For soft tissue-equivalent material, the distal fall-off edge of an in-room short acquisition is deeper compared to an off-line equivalent scan, indicating a better coverage of the high-dose end of the beam.

Conclusions—In-room PET is a promising low cost, high sensitivity modality for the in vivo verification of proton therapy. Better accuracy in Monte Carlo predictions, especially for biological decay modeling, is necessary.

Keywords

Proton therapy; in vivo range verification; in-room PET system; Monte Carlo simulation

1. Introduction

A proton beam has a finite range in the tissue and deposits most of its energy near the end of its track (Bragg peak). With no exit dose beyond the target, proton therapy is able to deliver highly conformal dose distributions in the tumor region compared to conventional external radiation treatment modalities such as X-ray, γ-ray or electron beam treatments, sparing

Corresponding author: Georges El Fakhri, Ph.D., Division of Nuclear Medicine, Department of Imaging, Massachusetts General Hospital. 55 Fruit Street, Boston, Massachusetts, the United States. Tel: 1-617-726-9640. Fax: 1-617-726-6165. elfakhri@pet.mgh.harvard.edu.

surrounding normal tissues, therefore is a favorable treatment modality for tumors with irregular shapes and near critical radiation sensitive structures. However, uncertainties in dose delivery can result from different sources, including treatment planning errors, beam delivery or patient positioning errors, organ motion, or for fractionated dose delivery, anatomic changes as a response to previous fractions. Proton range uncertainties are particularly of concern because of the large gradients of delivered dose near the Bragg peak, especially when there is a critical structure such as the spinal cord lying distal to the treatment planning target volume with a tight margin.

Positron emission tomography (PET) is a promising approach for in vivo and non-invasive range monitoring(Enghardt *et al.*, 2004; Parodi and Enghardt, 2000; Parodi *et al.*, 2007a; Parodi *et al.*, 2007b; Knopf *et al.*, 2009; Knopf *et al.*, 2008; Knopf *et al.*, 2010; Parodi *et al.*, 2008). During the treatment, small amounts of positron emitters, such as ^{11}C ($T_{1/2}$ = 20.39 min), ^{13}N ($T_{1/2}$ = 9.965 min), ^{15}O ($T_{1/2}$ = 2.037 min) and ^{38}K ($T_{1/2}$ = 7.636 min), are produced along the beam path via different channels of nuclear fragmentation reactions. PET measurement of thus endogenously produced activity has been proposed as a quality assurance method to ensure the proper functioning of treatment planning and beam delivery systems. Due to the high density of target nuclei in the tissue (>70% of oxygen in soft tissue) and the short half life of the final nuclei, usually ^{15}O is the dominant radionuclide immediately after proton irradiation. The distribution of activities depends on the beam flux, nuclear reaction cross sections and local target nuclei densities. In general the distribution of positron emitters is not proportional to the absorbed dose distribution. Due to the non-zero threshold energies of fragmentation reactions, there is no activation near the end of proton range. However, there is a unique relationship between the activity and dose distal fall-off positions, making range verification possible. Currently the verification is carried out by comparing PET images with predicted activity distributions calculated by Monte Carlo simulations. The range is verified by comparing the distal fall-off depths of activity distribution profiles between PET measurements and Monte Carlo predictions.

In-beam PET detectors inside the treatment room have been installed at two sites for carbon beam therapy (Pawelke *et al.*, 1997; Iseki *et al.*, 2003), with a third for proton therapy (Nishio *et al.*, 2010). In-beam detectors allow the real-time PET acquisition in the treatment position during the pauses of pulsed beam delivery and immediately after irradiation, therefore short-lived radionuclides such as ^{15}O can be detected. However, the integration of PET detectors into the beam delivery is technically challenging and subject to geometric constrains. The production of background radiation during beam extraction and sensitivity of PET imaging to the time course of irradiation require the synchronization of the PET data acquisition with the beam control system. Furthermore, in order to ensure an opening for the beam portal and flexible patient positioning, typically a dual-head system is the configuration of choice for an in-beam PET system. The limited solid angle for data collection results in not only reduced sensitivity but also severe artifacts in reconstructed PET images. The time-of-flight technique could be used to partially reverse the effects caused by non-complete angles of PET data collection(Crespo *et al.*, 2007), but also involves higher cost and implementation complexity. Due to the high cost and technical challenges associated with in-beam PET, up to data only one dedicated proton therapy facility (National Cancer Center, Chiba, Japan) has installed an in-beam PET system(Nishio *et al.*, 2010).

In the alternative offline operation modality, after treatment the patient proceeds to a nearby PET facility, usually a commercial full-ring PET scanner, for imaging. This method has been applied for 25 patients at our institution (Knopf *et al.*, 2009; Knopf *et al.*, 2010; Parodi *et al.*, 2007b). A PET/CT scanner is preferred for this purpose as accurate co-registration between treatment and imaging positions can be achieved. The offline approach is

technically less demanding, and better image quality can be achieved with a full-ring detector geometry configuration. Also the patient throughput in the treatment room is not affected, while in the in-beam scenario prolonged acquisition is required because of limited counting statistics. However, due to the delay required for patient transportation and repositioning, usually the short half-life radionuclides such as ^{15}O would have decayed, and only distribution of long half-life radionuclides (most importantly ^{11}C) can be measured. Additional errors are caused by patient repositioning and (in some sites) anatomical changes during the patient transportation and repositioning. More importantly, the biological washout of activity can significantly affect the spatial distribution of the signal (Parodi *et al.*, 2007b; Parodi *et al.*, 2008; Knopf *et al.*, 2009; Knopf *et al.*, 2010). In off-line studies done in the past at our institution, the average delay was 15 minutes between proton irradiation and PET acquisition, and the uncertainty on range verification was 1–2 mm in regions with low-perfusion, bony structures, and 4 mm in high-perfusion soft tissue regions(Knopf *et al.*, 2010).

We are investigating an in-room, stand-alone PET system which could potentially provide hospital-based proton centers with a cost-effective, high performance option for PET range verification. In-room PET overcomes the major limitations of both in-beam and off-line modalities. Compared to in-beam PET, an in-room stand-alone PET system involves a significantly lower cost, is more flexible and technically much easier to implement. A full-ring detector geometry can be used which improves both sensitivity (solid angle for data collecting efficiency) and image quality. Compared to off-line PET, instead of transporting and repositioning the patient at a remote site for imaging, with an in-room scanner the acquisition can be initiated very shortly (~2 minutes) after irradiation while short-lived nuclides are still abundant, and the overall signal intensity would be significantly higher than in the off-line scenario. In this work we report our first patient studies on proton range verification with an in-room PET system, compare the accuracy of in-room and off-line modalities quantitatively in a controlled phantom study, and identify limitations that need to be addressed in the future.

2. Methods

2.1. PET system

NeuroPET (PhotoDiagnostic Systems, Inc), a mobile PET scanner available at the Department of Imaging at Massachusetts General Hospital (MGH), was used in both patient and phantom studies. NeuroPET is a low-cost, high-sensitivity full-ring scanner with excellent flexibility. The scanner uses CsI(Na) scintillation material and Wavelength-shifting fiber technology to improve sensitivity and spatial resolution. PET images are reconstructed with a 3-D ordered subset Expectation Maximisation (OSEM) algorithm. Figure 1 showed NeuroPET positioned next to the beam nozzle in a proton therapy gantry treatment room at the Francis Burr Proton Therapy Center, Department of Radiation Oncology, MGH. Immediately following the completion of each treatment session, the treatment bed was rotated and translated to the PET scan position, without repositioning of the patient.

2.2. Subject selection and treatment

Two patients were enrolled into this pilot feasibility study with an Investigational Review Board (IRB) approved protocol. Both subjects were receiving fractionated proton radiation therapy at MGH in gantry-equipped treatment rooms. Both subjects were 49-year old females with adenoid cystic carcinoma, one in the nasopharynx and the other in the lacrimal gland. The total prescribed dose was 76 Gy(RBE) divided in 38 fractions of 2 Gy(RBE) each. Thermoplastic masks were used for patient immobilization.

2.3. Patient PET acquisitions and reconstructions

Each subject received two PET scans in list-mode after two treatment sessions ~1 week apart. For each session, the treatment and PET scan were taken on the same couch without patient repositioning. The irradiation, delay and scan times and other parameters are listed in table 1. The first scan of the first subject was 45 minutes to allow us to generate an off-line equivalent scan for comparison with in-room scans, as will be explained below. The second scan of the first patient was corrupted therefore not reported here.

Since NeuroPET does not have transmission imaging, we used CT images obtained off-line (treatment planning CT scans for patient studies) co-registered with the PET images for attenuation corrections and comparison between PET measurements and predictions. As radioactive markers were not allowed with the current IRB protocol, in patient studies we used a point source manually placed at several reference points around the empty masks for the co-registration of treatment planning CT and PET images. After releasing the subject, the empty mask was returned to the PET scan position and an additional 3-min PET scan was taken with a Ge-68 point source put briefly by hand next to each of several reference points on the mask. For the first subject, the reference points were chosen at several turning points on the mask recognizable in the CT scan, since no CT markers were available. For the second subject, 5 CT markers attached to the mask previous to the treatment planning CT scan were chosen as the reference points. CT scans for treatment planning were registered with non-attenuation corrected PET images through the reference points and were used to generate attenuation maps for patient PET scan reconstructions.

For the first scan of the first subject, the list-mode PET data were reconstructed into four typical time frames representing an in-room short acquisition (the first 5-min), an in-room long acquisition (first 30-min), an offline equivalent acquisition with a 15-min delay from the end of irradiation (minutes 14 to 44), and the sum (all 45-min). The PET data were also reconstructed into increasing time frame lengths from the beginning of the scan, representing in-room acquisitions of different lengths. The time frame lengths were incrementing in 1-minute steps for the first 6 minutes, then in 2-minute steps through the first 20 minutes, and in 5-minute steps afterwards. The coincidence count rates as a function of time were also extracted from the scanner for counting statistics analysis. For the two scans of the second subject, PET data were reconstructed for the first 5 minutes and for the entire 30-min acquisition.

2.4. Phantom construction

Figure 2 shows a sketch of the phantom used in our in-room PET study. The same phantom has been used for the study of cross sections for several PET activity production channels, which has been reported separately (Espana *et al.*, 2011). The phantom contained three different materials: high density polyethylene (HDPE), gelatinous water (water gel) and tissue equivalent gel (Tissue gel, with the same C/O ratio as in soft tissue). The dimensions were $12.7 \times 12.7 \times 5.1$ cm^3 for HDPE, and $12.7 \times 6.4 \times 5.1$ cm^3 for water gel and tissue gel. The material compositions and densities are given in table 2. The major reaction channels for positron-emitters production in phantom studies are listed in table 3.

2.5. Phantom irradiations and PET acquisitions

The phantom was irradiated in two studies with a 7 cm × 7 cm square aperture, as illustrated in figure 2. The range of the beams was 10.1 cm in water. In the first irradiation, a monoenergetic proton beam with 10.1 cm water-equivalent (WE) range was delivered. The radiation dose was 1.6 Gy at beam entrance. The phantom was irradiated for 168 seconds. After a 75-second delay, the phantom was imaged in NeuroPET for 38 minutes in list-mode. In the second irradiation, an SOBP field with a 10-cm WE range and a 6-cm modulation

(WE) was delivered. The radiation dose was 2.0 Gy at the spread-out peak region. The phantom was irradiated for 39 seconds. After a delay of 51 seconds, the phantom was imaged in NeuroPET for 45 minutes in list mode.

A CT image set of the phantom was taken with the Siemens Biograph 64 PET/CT scanner. The CT images were converted to attenuation maps and co-registered with non-attenuation-corrected PET reconstructions with concentric PET and CT markers for attenuation corrections.

2.6. Phantom PET reconstructions and data analysis

The list-mode PET data were reconstructed (1) with incrementing times from the beginning of acquisition, in 1-min steps for the first 10 min, 2-min step for the next 10 min, and 5-min steps thereafter, representing in-room scans with different acquisition lengths; (2) from 15 min to 38 (45) min, which is the equivalent of a 23(30)-min off-line scan, for the monoenergetic (SOBP) field.

Groups of activity profiles along the beam direction in the three materials were compared with Monte Carlo simulation results for general shapes and distal 50% fall-off depths for two time frames: in-room 5-minute and off-line 23 (30)-min reconstructions. Regions of activity profiles selection are illustrated in figure 2. The number of profiles was 100 for tissue and water gels, and 300 for HDPE. The distal 50% fall-off positions were calculated for each profile within the regions of selection. The mean value and standard deviation were calculated for each material.

2.7. Monte Carlo modeling

Since there is no direct correlation between the dose and activity distributions, expected β^+ activity distributions were calculated with Monte Carlo simulations to be compared with PET measurements. The predicted PET activity distributions were generated on CT scan grids. The code used for this study was developed by Paganetti *et al* (Paganetti *et al.*, 2008), based on Geant4 (Agostinelli and al, 2003). The general procedure followed to obtain the calculated PET images was similar to that explained by Parodi et al (Parodi *et al.*, 2007a), but with a few remarkable differences. First, a different set of cross section data was used (Espana *et al.*, 2011). Secondly, the modeling reported by Parodi et al employed FLUKA Monte Carlo code and used density corrections within the calculation to account for tissue with the same elemental composition but different density, while our implementation (Paganetti *et al.*, 2008) was done using Geant4 code and each tissue was individually defined with specific density and elemental composition according to Schneider et al (Schneider *et al.*, 2000). The activity concentration of the PET images was derived using eq. 1, in which the biological decay during the irradiation time was taken into consideration. The spatial resolution of the scanner was modeled as 7 mm of FWHM. The activity concentration on the Monte Carlo PET images can be derived as follows:

$$A(r)=G(r)\otimes\left\{\sum_i n_i \sum_j \sum_{k=f,m,s}\left[M_k(r)N_{ij}(r)\frac{1-\exp(-\lambda_{tot,j}(r)t_{irr,i})}{\lambda_{tot,j}(r)t_{irr,i}}\cdot\exp(-\lambda_{tot,j}(r)t_{del})\frac{1-\exp(-\lambda_{tot,j}(r)t_{scan})}{\lambda_{tot,j}(r)t_{scan}}\lambda_j/V_{voxel}\right]\right\} \quad (1)$$

where t_{irr} is the irradiation time, t_{delay} is the delay time, t_{scan} is the scan time, n_i is the normalization factor for the considered field (i), M_k (k = f(fast), m(medium), s(slow)) is the biologic decay fraction on each voxel (r), λ_j and $\lambda_{tot,j}$ are the isotope specific physical and total (i.e., physical plus biologic) decay constants respectively, N_{ij} is the total number of isotopes (j) produced for each field (i) in each voxel (r), and V_{voxel} is the volume of each individual voxel. The biological decay parameters were adapted from implanted ^{10}C and ^{11}C

pencil-beam animal study results (Mizuno *et al.*, 2003), as reported in our previous studies(Parodi *et al.*, 2007b; Parodi *et al.*, 2008). The number of protons at the entrance of the nozzle was $7.5 \cdot 10^8$ for each simulation.

3. Results

We present here first the three patient scans we have performed on two subjects in our pilot study, followed by the phantom study results to validate our approach and evaluate the best achievable range verification accuracies with different PET acquisition time schemes. Since NeuroPET does not have transmission imaging and radioactive markers were not allowed with the current IRB protocol, in patient studies large co-registration errors between PET and CT images were observed. Therefore, the PET activity distal fall-off depths in measurements and Monte Carlo predictions were not compared in details in patient studies. The estimated co-registration accuracies of immobilization masks in PET and CT images were listed in table 1. Additional errors between anatomical structures may exist, for example the displacement of patient head within the mask.

3.1. Counting statistics

A sample coincidence count rate (first subject, first scan) as a function of time for the patient scans are plotted in figure 3 (blue curve). As expected, the count rate decreased significantly in the first few minutes. Except for the first scan of the first subject (with a delay time of ~4 min between the end of irradiation and the start of PET acquisition), the coincidence count rate at the beginning of the in-room scan (with an average delay time of 2.5 min) was on average 11 times higher compared to the count rate at the projected starting time of an off-line equivalent scan. An in-room scan can greatly improve the counting statistics of the PET measurements. In terms of total coincidence counts, a short in-room scan of < 5 minutes is equivalent to an off-line scan of 30 minutes for a conservative 4-min delay.

3.2. Comparison of in-room PET (varied acquisition time frames) and off-line PET

Figure 3 shows the reconstructed PET images of four typical time frames for the first scan of the first subject. Visually inspecting, the image of a short in-room scan of 5 minutes has an activated volume with a better coverage of the high-dose region compared to an off-line equivalent scan of 30 minutes. The activated volume was calculated for regions with a PET activity higher than 5% of the average activity in the dose-penetrated region. The activated volume for the in-room short scan was 12% higher compared to the offline scan. Sample profiles reconstructed for incrementing acquisition lengths are shown in figure 4. In the brain region indicated with the arrow, the large peak obviously observable in short in-room scans disappeared in longer in-room scans and offline equivalent scans.

Figure 5 shows the PET images and sample profiles of the two scans of the second subject, reconstructed for the 5-minute and 30-minute acquisition times. The high activity in a soft tissue region in the 5-min short scan, as shown in the black ovals overlapping with the PET images, decreased dramatically for a 30-min long scan. From the corresponding activity profiles and the CT profile, it can be seen that for regions immediately upon the beam entrance (containing the thermoplastic mask, bony structures and fat tissues) the activity was well retained for both short and long scans (first peaks from the right); while for regions with brain or soft tissue, the highest peak observed in short scans (second from the right) almost disappeared in longer scans.

Figure 6 shows different time frame PET images for the second scan of patient 2. The total 30 min acquisition was split in 20 frames of 1 min each and 5 frames of 2 min. The purpose

of this figure was to illustrate the potential that in-room PET imaging is able to acquire an image in a much sorter period of time and with better contrast in the distal fall-off region.

3.3. Comparison of distal fall-off positions between PET measurements and Monte Carlo predictions

Figure 7 shows color wash images of the planned dose, PET images reconstructed for different time schemes and corresponding predictions from Monte Carlo simulations. The comparison of measured PET images of the same scan reconstructed for different time schemes is not affected by co-registration errors, while the comparisons between PET measurements and Monte Carlo predictions and among repeated scans are affected.

For Patient 1, a short 5-min in-room scan was compared with a 30-min off-line scan with a 15-min delay. Consistent with our previous observation, PET activities in the deeper soft-tissue region was better retained in the in-room short scan but disappeared in the off-line scan. For both time schemes, there is a larger disagreement between simulation and PET measurement in regions beyond the bone/fat layer. In additional to simulation and co-registration errors, possible causes also include errors in the biological washout model. More accurate modeling is necessary to predict PET distributions from simulations reliably. For Patient 2, a short (5-min) and a long (30-min) in-room scans were compared. The short and long in-room reconstructions have very similar coverage of the high-dose region near the end of the beam, but for the longer scan the relative activity concentration at the beam entrance is significantly higher compared to deeper soft-tissue regions, mostly due to high ^{11}C signals from the mask and bone/fat layer which were not subject to severe biological washout. When the PET measurements are compared with Monte Carlo predictions, it is interesting to note that an eye was in the beam path. While the eye has a very similar CT number as other brain/soft tissues, it has a much higher oxygen concentration. Also, the eye is not a perfused tissue and therefore not subject to severe biological washout. Therefore when the CT-based tissue-conversion and biological decay models were applied, the Monte Carlo simulation predicted activity concentration in the eye was significantly lower than in PET measurements.

While we have observed a large discrepancy between PET measurement and Monte Carlo prediction in the eye activity level, in an off-line study with an ocular melanoma patient reported by Parodi et al (2007b) the local activity maximum in the eye was well-reproduced by the Monte Carlo calculation. There are two possible reasons for the difference. First, in the ocular melanoma case the eye was the only target organ in the beam path, and dedicated choice of tissue segmentation and washout parameters were applied during Monte Carlo modeling. Also, since there was no other tissue activation for the comparison of relative activity levels, the relative activity distribution would not be changed even if a less accurate washout model was applied. Secondly, the prevailing signal is from ^{15}O in in-room studies and ^{11}C in off-line studies. This suggests that ^{15}O and ^{11}C have very different biological decay behavior and should be treated differently, especially for tissues with high oxygen concentrations such as the eye.

3.4. Phantom studies

The in-room phantom measurements were used in extensive studies for the selection and validation of cross section data for Monte Carlo simulations(Espana *et al.*, 2011), the results of which were used in all the Monte Carlo simulations in this study. Sample profiles along the beam directions for the tissue gel are shown in figure 8 for in-room 5-min acquisitions and off-line acquisitions. The difference of 50% distal fall-off measurements between PET measurements and Monte Carlo predictions was 0.2 ± 0.5 mm (monoenergetic) and 0.8 ± 0.5 mm (SOBP) for the in-room short scan, and 2.1 ± 0.5 mm (monoenergetic) and 4.4 mm ±

0.5 (SOBP) for the off-line scan. For the monoenergetic beam irradiation, the activity profile of the in-room short scan has a steeper distal fall-off gradient compared to the off-line scan. This could because while ^{15}O from the $^{16}O(p, pn)^{15}O$ reaction is the dominate contribution in a short in-room scan, in an off-line scan the activity profiles usually contain contributions from several reaction channels such as $^{12}C(p, pn)^{11}C$, $^{16}O(p, 3p3n)^{11}C$, $^{16}O(p, 2p2n)^{13}N$, etc., with different threshold energies, therefore the mixture has a shallower gradient. The shape of cross section vs. energy curve of the $^{16}O(p, 3p3n)^{11}C$ channel (Espana *et al.*, 2011) has a slightly slower rising edge, which also contribute to the shallower distal gradient of off-line profiles. The steeper distal region in the in-room scan could potentially reduce the uncertainty in distal fall-off determination through gradient analysis. The 50% distal fall-off depths were calculated and compared with simulation results in figure 9. For water and tissue gels, the distal fall off depths for an in-room 5-min scan were deeper than in a longer off-line scan, indicating the activated field has a better coverage of the high-dose region in a short in-room scan. Please note that above findings only apply to the situations when the proton beam ends in oxygen-rich tissues such as the soft tissue, not in less frequent carbon-rich or bony tissues such as in the case of some head and neck tumors(Knopf *et al.*, 2009).

The mean values and standard deviations of 50% distal fall-off depth for each material were calculated and plotted as a function of reconstruction time length in figure 10 (monoenergetic). For HDPE, the distal fall-off depth was similar for all reconstruction time lengths and the off-line measurement. The standard deviation decreased continuously as a function of reconstruction lengths, since there is only one possible reaction channel (i.e. the shape of profiles is the same for all the time frames) and distal fall-off depth uncertainty depends on image noise only. For water and tissue gels, the distal fall-off depth of short in-room scans was 2~3.5 mm deeper compared to the off-line scan. The fall-off depth decreased slightly for longer in-room scans. The standard deviation decreased rapidly at the beginning as ^{15}O was the only dominant for the first few minutes, reaching a minimum at 3~6 min, then started increasing again for tissue gel since the increasing contributions from longer half-life nuclides (^{11}C and ^{13}N) changed the gradients of the distal fall-off region. The standard deviations of off-line measurements were 0.8~0.9 mm larger than that of 3~5-min in-room measurements. The mean values and standard deviations of distal fall-off depth was also calculated for the SOBP study, and plotted in figure 11. A similar trend was observed in the change of mean distal fall-off depth values, but with smaller amplitude, since the profiles involve productions from a mixture of proton energies. For tissue gel, the standard deviations for distal fall-off changed only slightly when the in-room acquisition length increased.

4. Discussion

In-room, stand-alone PET system is a promising alternative to the current in-beam and off-line modalities for range verifications in proton therapy. Compared to an in-beam PET system, a stand-alone PET scanner within the treatment room involves a significantly lower cost and is expected to have better image quality from complete tomographic data. In this study we compared the performance of in-room PET with systematically generated off-line equivalent studies. Please note that actual off-line studies also involve repositioning errors that were not reflected in our off-line equivalent reconstructions.

We have shown in our pilot phantom and patient studies that with an in-room scanner it is feasible to reduce the delay between irradiation and PET scan from 15 minutes (off-line) to 2.5 minutes, which can greatly improve the counting statistics of the PET measurements. This allowed us to decrease PET acquisition time to ~ 5 minutes (from 30-min in off-line modality) while still achieving equivalent or better accuracy in distal fall-off determination. Other than improved counting statistics, the additional benefits of a short in-room scan in a

soft tissue region (compared to an off-line scan) include (1) a better coverage of high-dose region. The distal fall-off depth of ^{15}O is closer to the dose fall-off edge, covering a larger portion of the high-dose SOBP region; (2) a steeper distal fall-off region in activity profiles in soft tissue. Because of the limited spatial resolution of PET imaging modality, higher accuracy in range verification is achieved through the gradient analysis in the distal fall-off region, and a steeper gradient can reduce the uncertainty of distal fall-off depth determination. When using gradient analysis for distal fall-off depth comparison, the activity threshold should be chosen carefully so that the depths are compared close to the distal edge with the largest gradient, where the most robust result is expected.

With an in-room scanner both ^{15}O and ^{11}C signal will be collected. The ^{15}O intensity is very high immediately after irradiation, but because of its short half life, after a few minutes most of the ^{15}O decays, and ^{11}C becomes the dominate nuclide. Therefore ^{15}O is the most important contribution in a short scan, but for a longer acquisition the relative contribution of ^{11}C increases substantially. Biologically, soft tissue/brain regions have higher oxygen composition (therefore higher ^{15}O production) and suffer from faster biological washout of activity because of higher perfusion. A short scan involves less activity washout, in contrast with a longer scan where the much higher washout of later time is averaged into the final reconstruction.

In our first experience of in-room PET with NeuroPET, the largest technical obstacle is the co-registration accuracy between PET and CT image sets, which is essential for the accurate comparison of PET measurements and Monte Carlo predictions. Patient setup errors and anatomic changes could also be a great contribution of co-registration uncertainty. Therefore, PET/CT is very desirable for in-room PET verification of proton therapy. We will receive the second generation of NeuroPET in the near future, which will also include a CT component. We expect greatly improved co-registration accuracy in future studies.

We have also encountered several theoretical obstacles in the modeling of expected PET activity distributions. The Monte Carlo modeling of PET activity production depends on the correct assignment of tissue density/composition at the voxel level, as well as reliable nuclear reaction cross section data. A variety of experimental and evaluated values for cross sections of different reaction channels have been published (EXFOR, 2010; ICRU, 2000), however there are significant discrepancies between different data sets. More accurate measurement of cross section values is very desirable. Currently we are using a CT conversion algorithm used in clinical treatment planning for voxel-by-voxel tissue type assignment. However, besides CT noise and artifacts, some tissue types with similar CT numbers may have very different elemental compositions, and incorrect assignment of tissue parameters could cause large errors in activity production calculations. For the modeling of biological washout of activity, the current washout model was developed based on animal studies with implanted ^{10}C and ^{11}C beams (Mizuno *et al.*, 2003), which is not suitable for proton induced activity, especially for the early time frames when ^{15}O dominants. More accurate modeling of biological washout for ^{15}O is necessary for the correct prediction of in-room activity distributions. In addition, tissue types with similar CT numbers could have completely different biological washout rates. In our second patient study, one eye was in the beam path. The eye has very similar CT number to soft tissue, but with very different composition (much higher oxygen composition) and no biological washout at all, therefore using CT number as the reference for tissue type assignment and biological washout correction caused significant errors. Prior information should be applied to ensure the correct tissue types and washout rates are applied to different tissue types.

The major drawback of the in-room PET modality is that it will affect patient throughput in the proton therapy treatment room as an in-room scan requires extended stay of the patient

after therapy. However, due to the significantly reduced PET acquisition time (<=5 min), we consider this to be acceptable because the verification will only need to be performed for clinical conditions that proton range is a known problem. Also, for fractionated treatments usually no repeated verification is necessary after the first treatment session unless a problem is found or if there is a change in the treatment plan. Secondary, due to the fast decay of ^{15}O, in-room PET is sensitive to the timing of PET acquisitions because the shape of activity profiles can be greatly affected by the mixing ratios of radionuclides with different half lives.

In-room PET allows new potentials for personalized proton therapy treatment, such as verification of individual fields in a multiple-field irradiation and real-time adaptive monitoring of therapy. To achieve adaptive monitoring with in-room PET, a small fraction of the planned dose is delivered first, followed by a quick PET scan, and then the patient is moved back to the treatment position. The complete dose is delivered only after the proton beam range has been verified. These practices require exchanges between treatment and scan positions, therefore are usually impossible or very difficult with an offline scanner because imaging is performed at a remote site.

5. Conclusions

In-room PET is a promising low cost, high sensitivity modality for the in vivo verification of proton therapy. Our pilot study showed that compared to off-line PET, the acquisition time can be greatly reduced from 30 min to 5 min with an in-room scanner, and signal in high-perfusion soft tissue and brain region can be better retained. Better accuracy in Monte Carlo predictions, especially for biological decay modeling, is necessary.

Acknowledgments

NIH/NCI PO1 CA02139-29 "Proton Therapy Research"

NIH/NIBIB T32 EB002102

References

Agostinelli S, et al. Geant4 - a simulation toolkit. Nucl Instrum Methods Phys Res A. 2003; 506:250–303.

Crespo P, Shakirin G, Fiedler F, Enghardt W, Wagner A. Direct time-of-flight for quantitative, real-time in-beam PET: a concept and feasibility study. Phys Med Biol. 2007; 52:6795–6811. [PubMed: 18029976]

Enghardt W, Parodi K, Crespo P, Fiedler F, Pawelke J, Ponisch F. Dose quantification from in-beam positron emission tomography. Radiother Oncol. 2004; 73 Suppl 2:S96–S98. [PubMed: 15971319]

Espana S, Zhu X, Daartz J, El Fakhri G, Bortfeld T, Paganetti H. The reliability of proton-nuclear interaction cross-section data to predict proton-induced PET images in proton therapy. Phys Med Biol. 2011; 56:2687–2698. [PubMed: 21464534]

EXFOR. Energy Sciences and Technology Dept., BNL. 2010. http://www.nndc.bnl.gov/nndc/exfor/:

ICRU. Tissue Substitutes in Radiation Dosimetry and Measurement. Bethesda, MD: International Commission on Radiation Units and Measurements; 1989.

ICRU. Nuclear Data for Neutron and Proton Radiotherapy and for Radiation Report No 63. Bethesda, MD: 2000.

Iseki Y, Mizuno H, Futami Y, Tomitani T, Kanai T, Kanazawa M, Kitagawa A, Murakami T, Nishio T, Suda M, Urakabe E, Yunoki A, Sakai H. Positron camera for range verification of heavy-ion radiotherapy. Nucl Instrum Methods A. 2003; 515:840–849.

Knopf A, Parodi K, Bortfeld T, Shih HA, Paganetti H. Systematic analysis of biological and physical limitations of proton beam range verification with offline PET/CT scans. Phys Med Biol. 2009; 54:4477–4495. [PubMed: 19556685]

Knopf A, Parodi K, Paganetti H, Cascio E, Bonab A, Bortfeld T. Quantitative assessment of the physical potential of proton beam range verification with PET/CT. Phys Med Biol. 2008; 53:4137–4151. [PubMed: 18635897]

Knopf AC, Parodi K, Paganetti H, Bortfeld T, Daartz J, Engelsman M, Liebsch N, Shih H. Accuracy of Proton Beam Range Verification Using Post-Treatment Positron Emission Tomography/ Computed Tomography as Function of Treatment Site. Int J Radiat Oncol Biol Phys. 2010

Mizuno H, Tomitani T, Kanazawa M, Kitagawa A, Pawelke J, Iseki Y, Urakabe E, Suda M, Kawano A, Iritani R, Matsushita S, Inaniwa T, Nishio T, Furukawa S, Ando K, Nakamura Y, Kanai T, Ishii K. Washout measurement of radioisotope implanted by radioactive beams in the rabbit. Phys Med Biol. 2003; 48:2269–2281. [PubMed: 12953897]

Nishio T, Miyatake A, Ogino T, Nakagawa K, Saijo N, Esumi H. The development and clinical use of a beam ON-LINE PET system mounted on a rotating gantry port in proton therapy. Int J Radiat Oncol Biol Phys. 2010; 76:277–286. [PubMed: 20005459]

Paganetti H, Jiang H, Parodi K, Slopsema R, Engelsman M. Clinical implementation of full Monte Carlo dose calculation in proton beam therapy. Phys Med Biol. 2008; 53:4825–4853. [PubMed: 18701772]

Parodi K, Bortfeld T, Haberer T. Comparison between in-beam and offline positron emission tomography imaging of proton and carbon ion therapeutic irradiation at synchrotron- and cyclotron-based facilities. Int J Radiat Oncol Biol Phys. 2008; 71:945–956. [PubMed: 18514787]

Parodi K, Enghardt W. Potential application of PET in quality assurance of proton therapy. Phys Med Biol. 2000; 45:N151–N156. [PubMed: 11098922]

Parodi K, Paganetti H, Cascio E, Flanz JB, Bonab AA, Alpert NM, Lohmann K, Bortfeld T. PET/CT imaging for treatment verification after proton therapy: a study with plastic phantoms and metallic implants. Med Phys. 2007a; 34:419–435. [PubMed: 17388158]

Parodi K, Paganetti H, Shih HA, Michaud S, Loeffler JS, DeLaney TF, Liebsch NJ, Munzenrider JE, Fischman AJ, Knopf A, Bortfeld T. Patient study of in vivo verification of beam delivery and range, using positron emission tomography and computed tomography imaging after proton therapy. Int J Radiat Oncol Biol Phys. 2007b; 68:920–934. [PubMed: 17544003]

Pawelke J, Enghardt W, Haberer T, Hasch BG, Hinz R, Kramer M, Lauckner E, Sobiella M. In-beam PET imaging of the control of heavy-ion tumour therapy. IEEE Trans. Nucl. Sci. 1997; 44:1492–1498.

Schneider W, Bortfeld T, Schlegel W. Correlation between CT numbers and tissue parameters needed for Monte Carlo simulations of clinical dose distributions. Phys Med Biol. 2000; 45:459–478. [PubMed: 10701515]

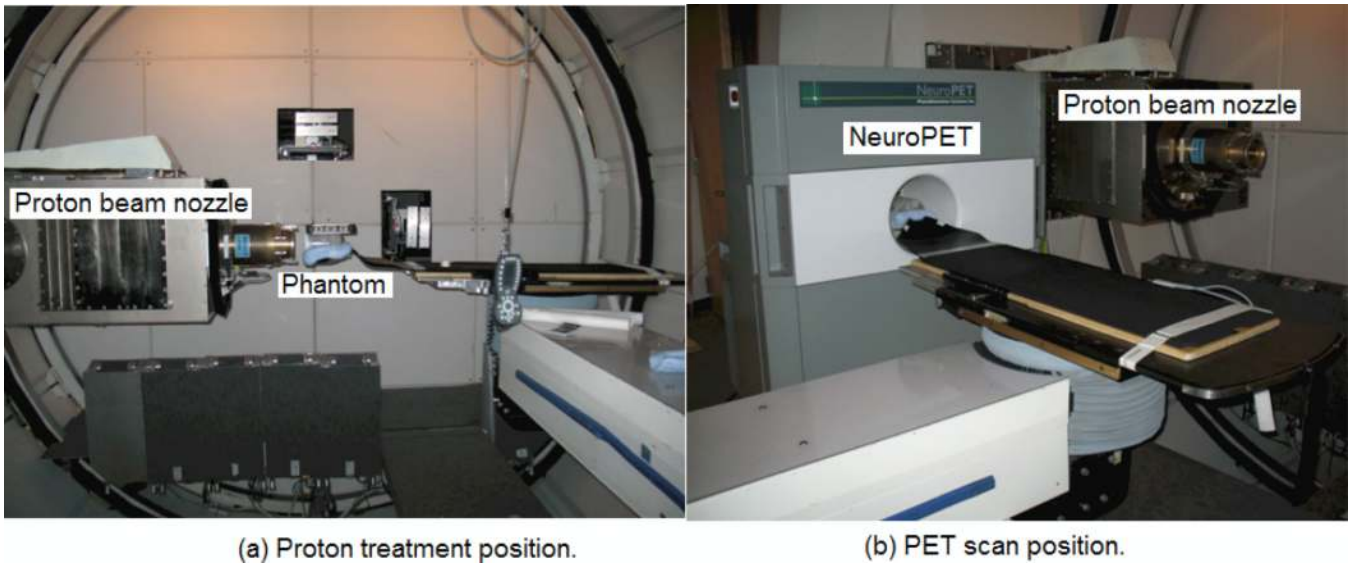

Figure 1.
Treatment bed in the (a) proton treatment and (b) PET scan positions during an in-room phantom study. After beam delivery, the treatment bed was rotated and translated, and the phantom was inserted directly into the scanner for the PET scan.

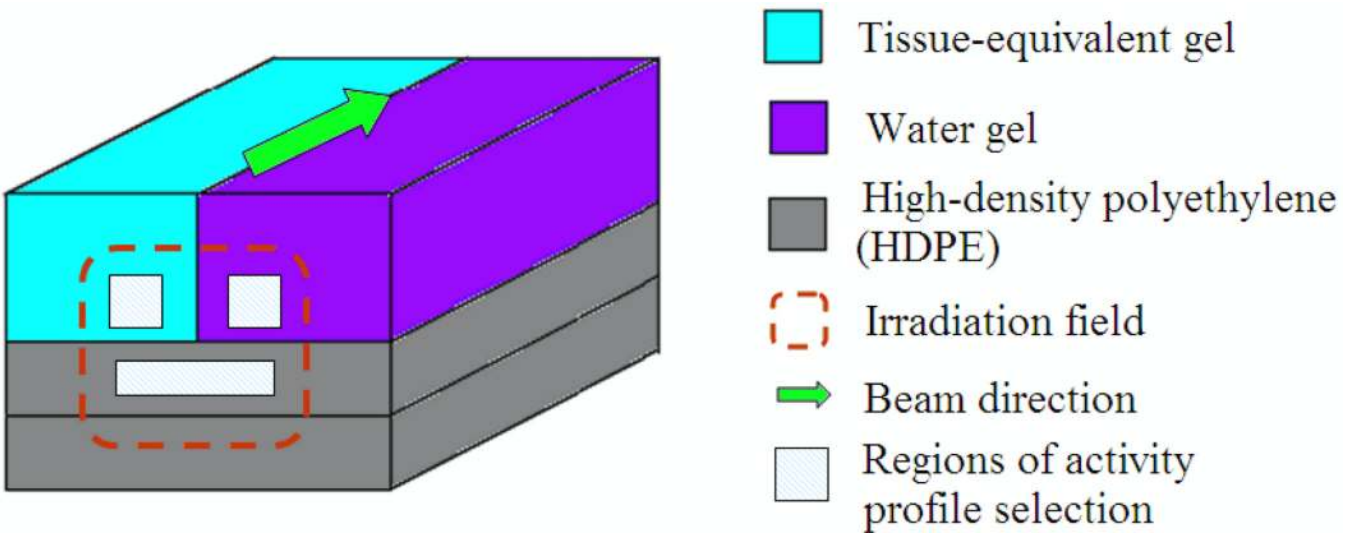

Figure 2.
The phantom used in the in-room study. The phantom was constructed with three materials, for the parallel study of the proton activation of carbon-only and almost oxygen –only materials, as well as a tissue-equivalent material with a realistic carbon/oxygen ratio. The dimensions of the phantom are 12.7 × 12.7 × 10.2 cm^3. The compositions of the three materials are given in table 2.

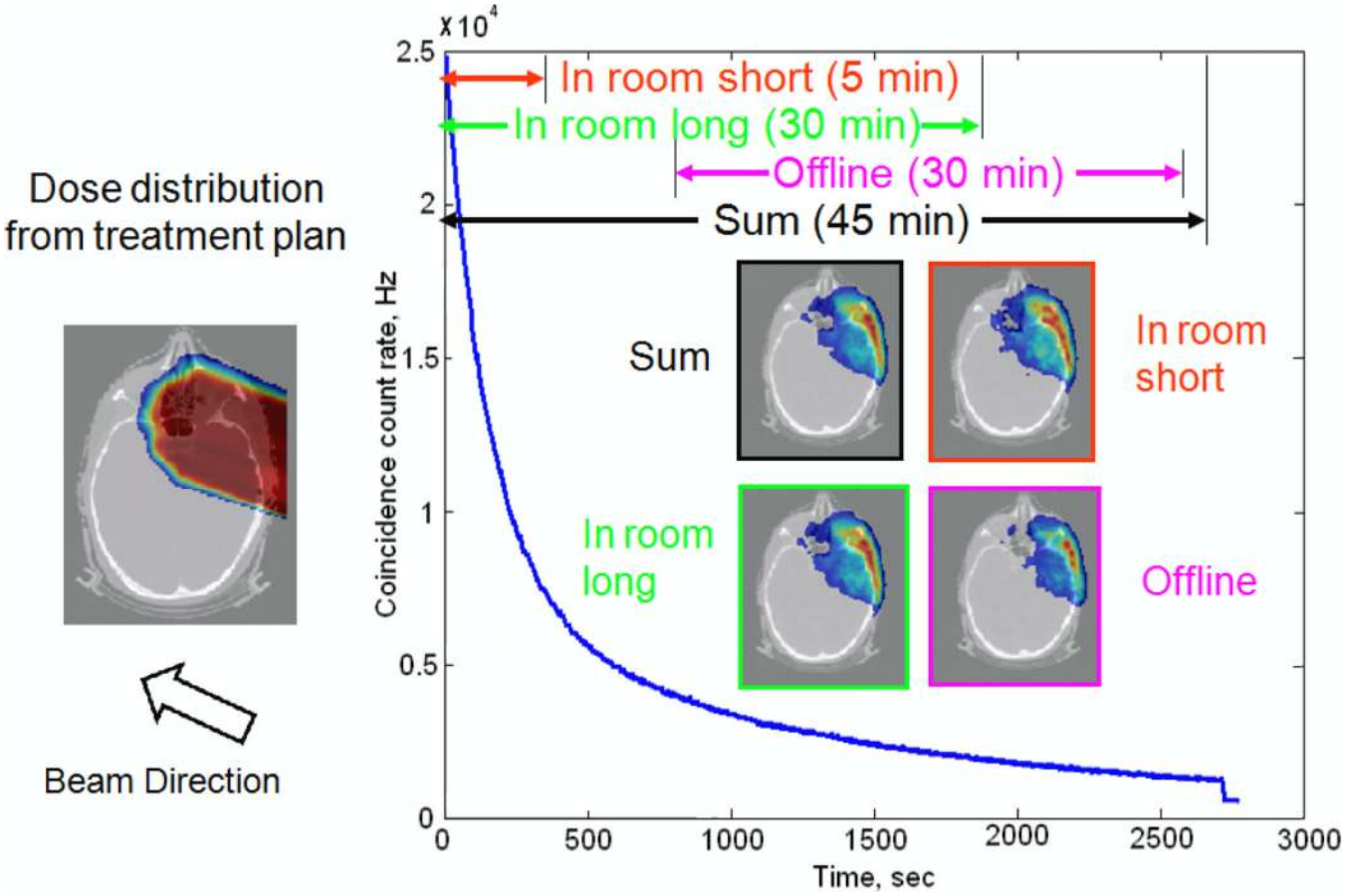

Figure 3.
Patient study: first subject, first scan. The blue curve is the coincidence count rate as a function of time. The dose distribution of a sample slice is shown on the left. The corresponding PET images reconstructed for the four time frames on the top (with individually normalized color scale) are shown as inserts (right).

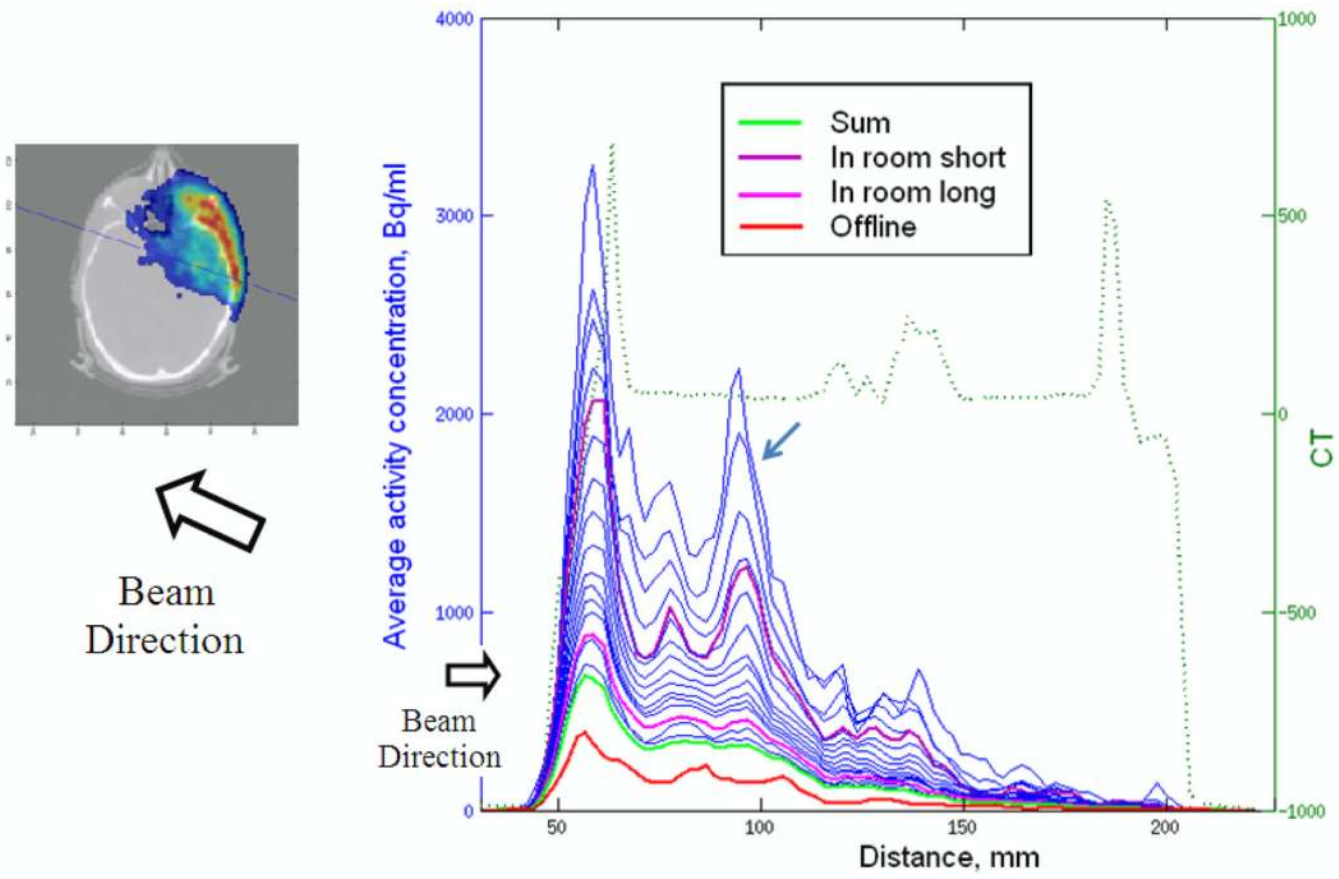

Figure 4.

Sample PET activity profiles of the first scan of the first patient, reconstructed for incrementing in-room acquisition lengths and off-line equivalent time frames. The profile location is shown on the left. The blue curves on the right, from top to bottom, are reconstructed activity profiles for incrementing in-room acquisition lengths from 1 minute to 45 minutes (See reconstruction schemes in the Methods section). The activity profiles for the four typical frames are shown in different colors. The green dotted curve is the CT profile. The peak in the brain region in short in-room scans indicated by the arrow disappeared in longer in-room scans and the off-line equivalent scan.

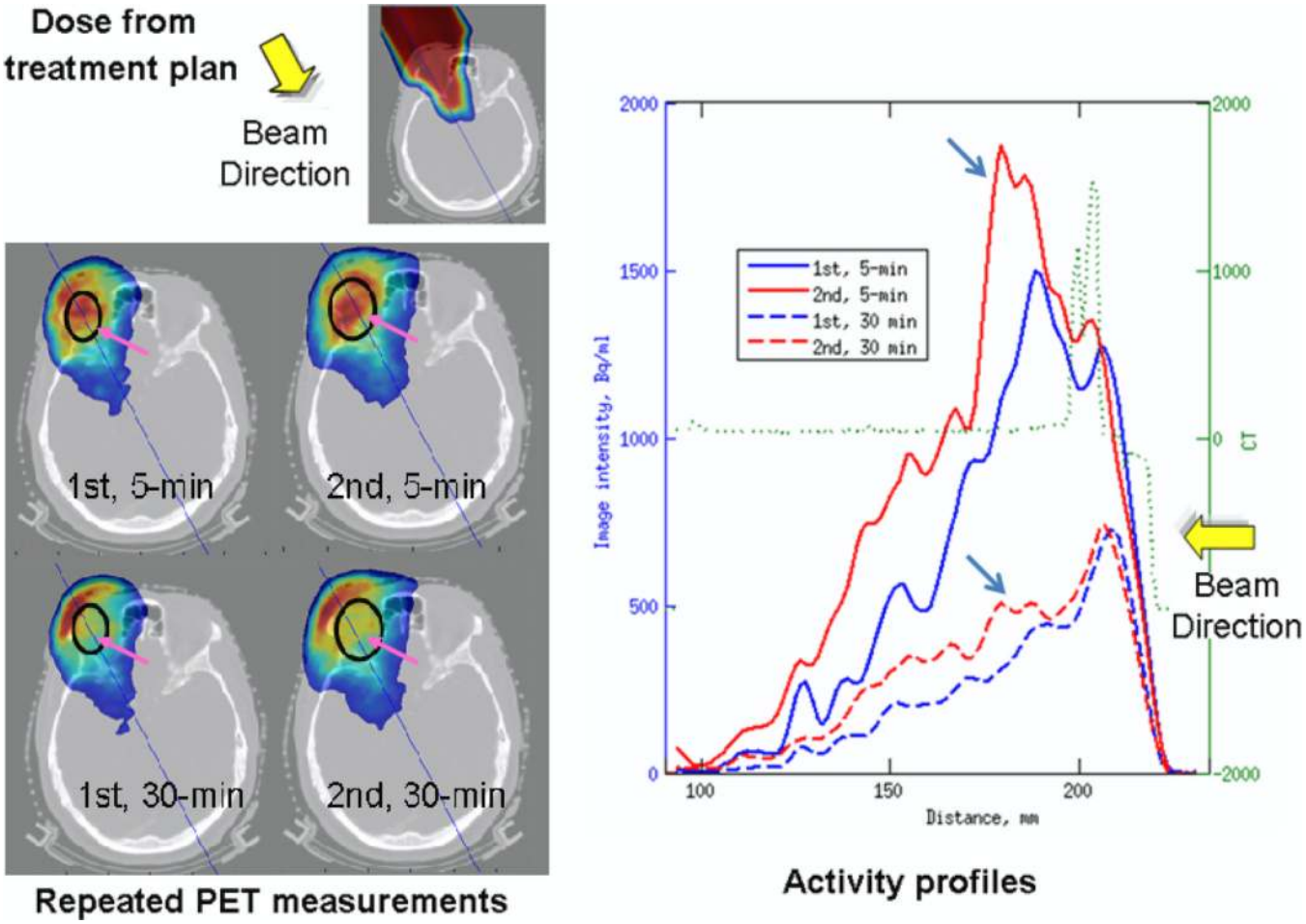

Figure 5.

Repeated scans of the second subject showing the retaining of activity in soft tissue/brain region for short in-room PET scans. The subject was scanned twice, 1-week apart, for two fractionated sessions of the same treatment plan. The listmode data were reconstructed for the first 5 minutes, or the entire 30 minutes. The high activity in a soft tissue region in the 5-min short scan, as shown in the black ovals overlapping with the PET images, decreased dramatically for a 30-min long scan. The corresponding activity profiles (solid for short 5-min, dashed for long 30-min, blue for the first and red for the second scans) and the CT profile (green dotted curve) are shown on the right. For regions with bony structures and fat tissues the activity was well retained for both short and long scans (first peaks from the right); while for regions with brain or soft tissues, the highest peak observed in 5-min scans (second from the right) almost disappeared in 30-min scans.

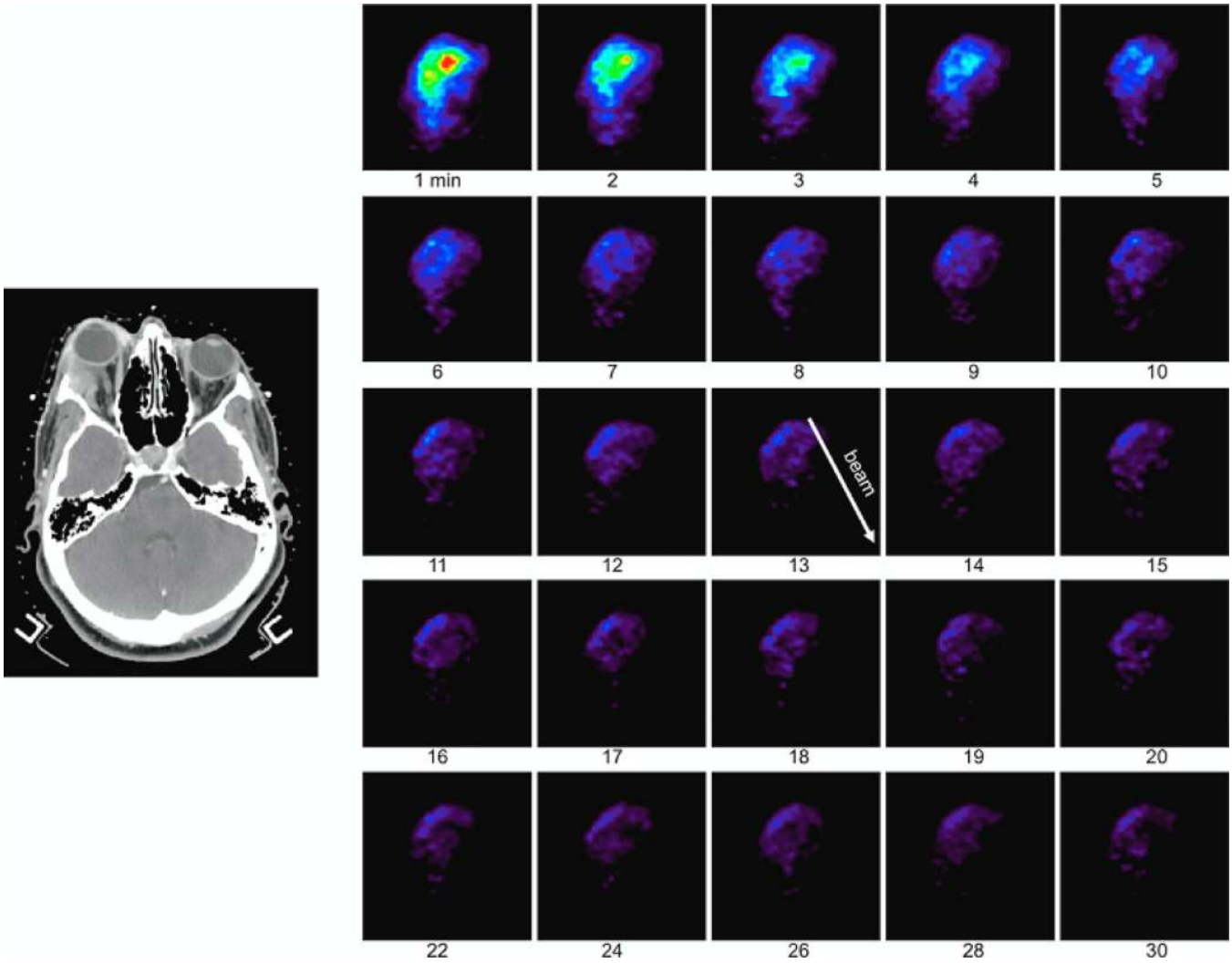

Figure 6.
Transverse view of the PET images obtained for the second scan of patient 2. Each image represents a different time frame starting on the top left corner with 1 min duration up to 20 min and 2min duration from 20 to 30 min.

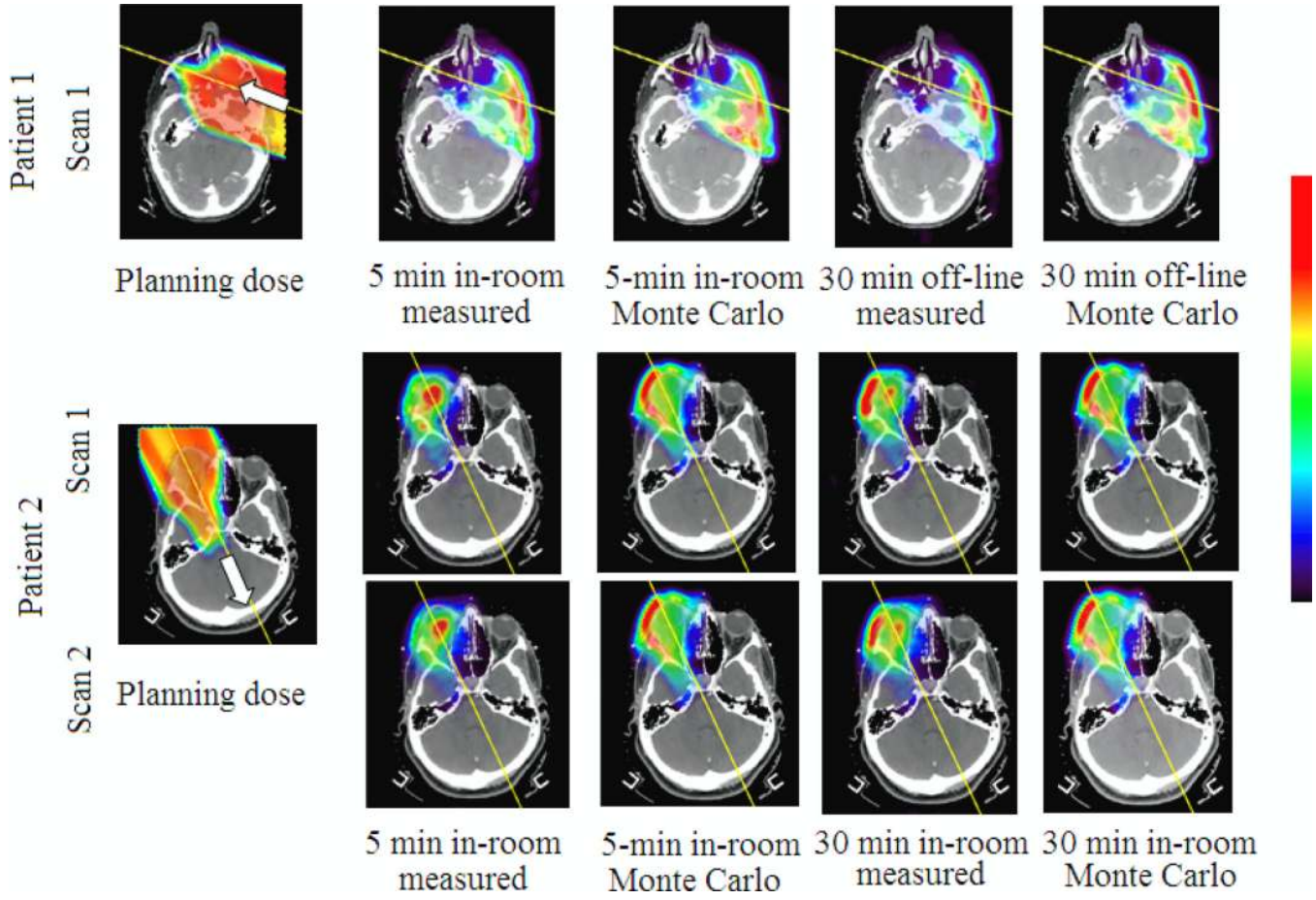

Figure 7.
Planning dose (left column) images and measured and Monte Carlo PET images for different acquisition protocols for patients 1 and 2. Color scale was independently normalized for each image. The white block arrows indicate beam directions in the planning dose images.

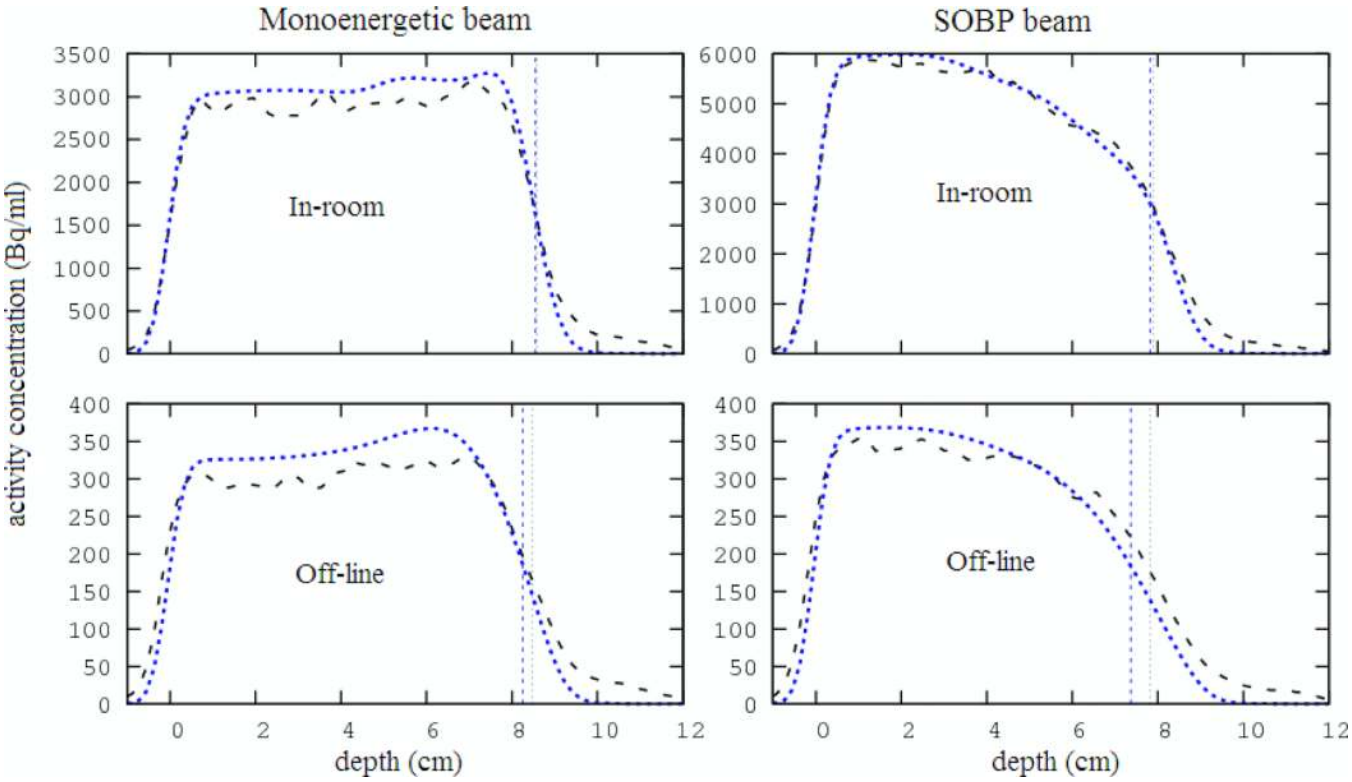

Figure 8.
Activity profiles of in-room short and off-line equivalent acquisitions for tissue gel. The black dashed curves are PET measured activity profiles and blue dotted curves are Monte Carlo predictions. The vertical lines indicate the distal 50% fall-off positions.

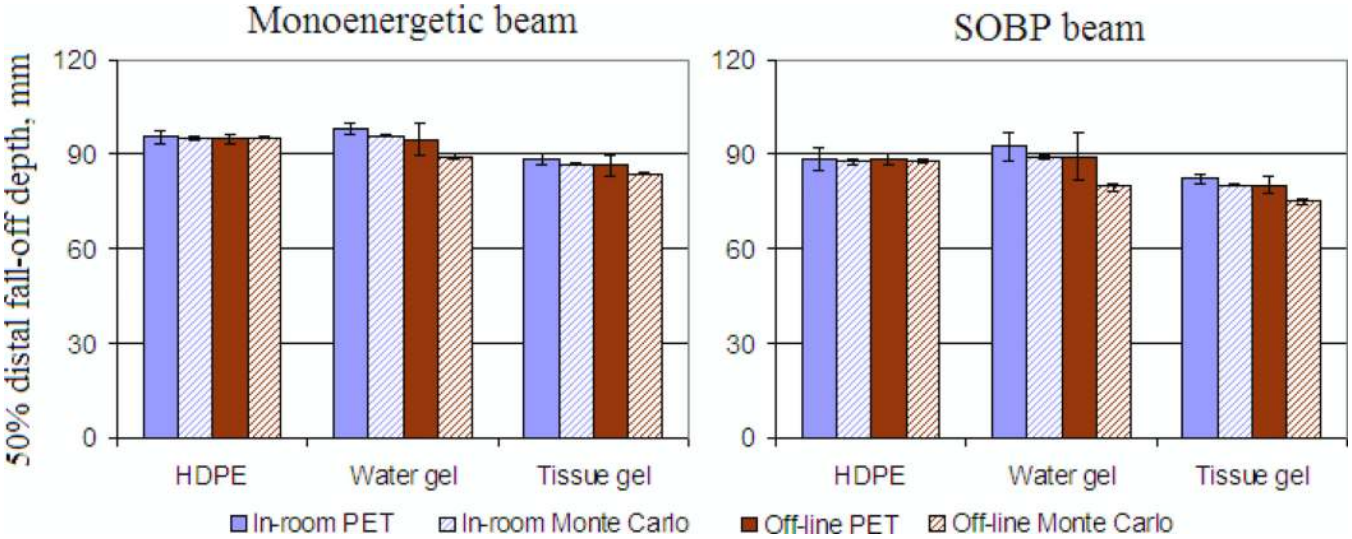

Figure 9.

Distal 50% fall-off depths (mm) in phantom studies. In-room measurements were with ~2-min delay and 5-min PET acquisition. Off-line equivalent measurements were with 15-min delay and 23/30 min (monoenergetic/SOBP) acquisition time.

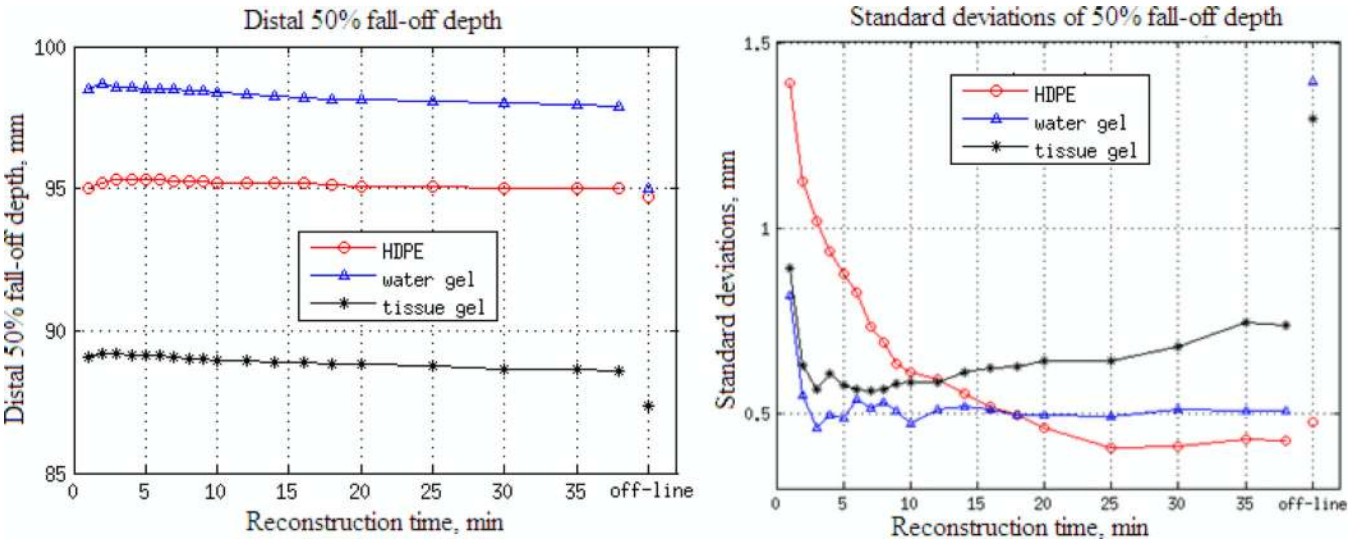

Figure 10.
Distal 50% fall-off depths as a function of reconstruction time, monoenergetic beam.

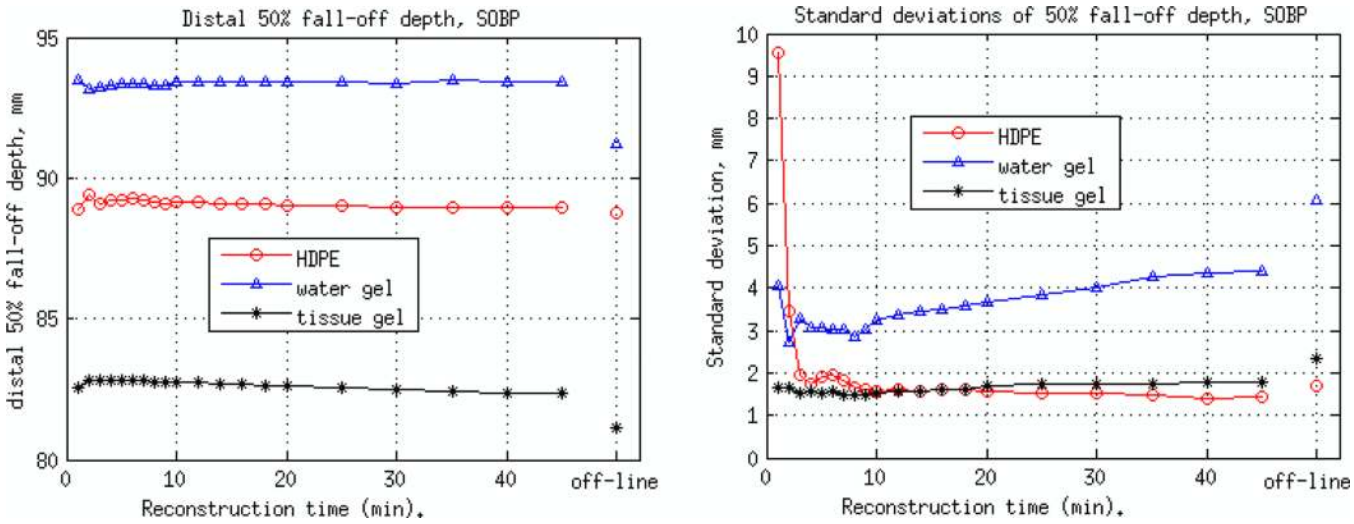

Figure 11.
Distal 50% fall-off depths as a function of reconstruction time, SOBP beam.

Table 1

Proton treatment and PET scanning information for patient studies.

	Patient 1	Patient 2	
Tumor	adenoid cystic carcinoma	adenoid cystic carcinoma	
Location	nasopharynx	lacrimal gland	
Number of fields	1	1	
Prescribed dose (Gy(RBE))	2	2	
Range/Modulation (mm)	125 / 100.4	117 / 114	
Scan #	1	1	2
Irradiation time (s)	23	30	73
Delay time (s)	204	170	149
Scan time (min)	45	30	30
Reconstruction method	3D-OSEM 5 iterations, 4 subsets, 0.3 mm Gaussian filter		
Coreg. Accuracy (mm)	5.5	3.5	
Images	128×128×128 voxels, 2×2×1.925 mm^3 each		

Table 2

Density and elements weight fraction of the three materials in phantom.

Material	H (%)	C (%)	N (%)	O (%)	O/C	Density (g/ml)
Soft tissue *	10.2	14.3	3.4	70.8	4.95	1.06
HDPE	14.3	85.7	0.0	0.0	0	0.95
Gel-tissue	9.6	14.9	1.46	73.8	4.95	1.13
Gel-water	11.03	1.04	0.32	87.6	84.2	1.01

* ICRU Report #44 (ICRU, 1989)

Table 3

Reaction channels and positron-emitters production in phantom materials

material	Nuclear reaction channels	End products
HDPE	$^{12}C(p,pn)^{11}C$	^{11}C
Water gel	$^{16}O(p,pn)^{15}O$, $^{16}O(p,2p2n)^{13}N$, $^{16}O(p,3p3n)^{11}C$	^{15}O, ^{11}C, ^{13}N
Tissue gel	$^{16}O(p,pn)^{15}O$, $^{16}O(p,2p2n)^{13}N$, $^{16}O(p,3p3n)^{11}C$ $^{12}C(p,pn)^{11}C$ $^{14}N(p,pn)^{13}N$, $^{14}N(p,2p2n)^{11}C$	^{15}O, ^{11}C, ^{13}N